Materials Research. 2023; 26: e20220500
DOI: https://doi.org/10.1590/1980-5373-MR-2022-0500

Change with the Reactive Deposition Mode in Crystallographic and Mechanical Properties of Titanium Aluminum Nitride Coatings Obtained Via Grid-Assisted Magnetron Sputtering

Marcio Luiz Moretti[a] **,** ***Julio Cesar Sagas***[a]**,** ***Abel Andre Candido Recco***[a*]

[a]*Universidade do Estado de Santa Catarina, Departamento de Fisica, Paulo Malschitzki, 200, Zona Industrial Norte, 89219-710, Joinville, SC, Brasil.*

Received: November 25, 2022; Revised: March 20, 2023; Accepted: April 13, 2023.

Thin films of titanium aluminum nitride ($Ti_{(1-x)}Al_xN$) were deposited on silicon, copper, and plasma nitrided AISI D2 tool steel substrates through reactive direct current grid-assisted magnetron sputtering. The depositions were performed in the metal and compound modes using nitrogen flow rates of (7.2 ± 0.1) sccm and (6.8 ± 0.2) sccm, respectively. The relations between the process parameters and the crystallographic orientation were investigated. Chemical and mechanical properties were characterized by X-ray photoelectron spectroscopy (XPS), X-ray diffraction (XRD), scanning electron microscopy (SEM), transmission electron microscopy (TEM), and instrumented indentation technique (IIT). X-ray diffraction spectra and electron diffraction patterns revealed the presence of a $Ti_{(1-x)}Al_xN$ phase with a face-centered cubic structure in both films. In metal mode, the coatings exhibited a preferential (111) plane orientation, changing to (200) in the compound mode. The change in preferential orientation was influenced by the reactive gas partial pressure.

Keywords: *$Ti_{(1-x)}Al_xN$, Grid-assisted magnetron sputtering, Reactive sputter deposition, Crystallographic orientation.*

1. Introduction

Titanium aluminum nitride ($Ti_{(1-x)}Al_xN$) coatings are widely used in many industrial applications, such as dies, chucks, and cutting tools[1-3]. $Ti_{(1-x)}Al_xN$ has high hardness, wear resistance, oxidation resistance, and low coefficient of friction[4]. Titanium and aluminum nitrides are synthesized by various techniques, among which plasma-assisted chemical vapor deposition[5] and reactive sputtering deposition[6-8] stand out.

The reactive sputtering deposition is characterized by the hysteresis of the process parameters as a function of the reactive gas flow rate[9]. The hysteresis process can be divided into two well-defined modes: metal and compound[10]. In the metal mode, all reactive gas flow inserted in the system is consumed at the condensation sites. As a result, sub-stoichiometric films with a high deposition rate are produced[9]. This situation remains until the system reaches the first critical point (FCP). Stoichiometric films are grown near the FCP[9]. Increasing the reactive gas flow rate beyond the FCP, the consumption rate decreases and the excessive reactive gas leads to an abrupt increase in pressure. In addition, the compound fraction on the target surface increases, leading to the so-called target poisoning, which changes the plasma due to the change in the secondary electron emission coefficient and sputtering yield. Subsequently, the system enters the compound mode, in which stoichiometric films with a low deposition rate are produced[9,11]. Decreasing the reactive gas flow, the second critical point (SCP) occurs at a flow rate lower than the FCP, where the target is de-poisoned and returns to the metal mode[9].

*e-mail: abel.recco@udesc.br

The development of the preferential crystallographic orientation in titanium nitride (TiN) and $Ti_{(1-x)}Al_xN$ films strongly depends on process parameters, such as the nitrogen (N_2) flow[12,13], the reactive gas pressure[13], substrate temperature[13], and the substrate bias voltage[3,13,14]. In addition, other factors also influence the development of the preferential plane, such as the target's chemical composition[15] and the coating thickness[13,16,17].

Table 1 shows the correlation between the described parameters and the preferential orientation.

The increase of N_2 partial pressure[13] or N_2 gas flow rate[12,13] can lead to a change of preferential orientation from the (111) plane to the (200) plane. Earlier models claim that this is caused by the competition between the deformation and the surface energies of the coatings. When the deformation energy is predominant, favorable growth occurs in the (111) plane orientation. However, when the surface energy predominates, the preferential orientation is (200)[13]. On the other hand, more recent models associate this transition with the increase in the atomic N/Ti flux[13]. The increase in the substrate temperature[13] and substrate bias voltage[3,13,14] also promotes the transition of the preferential plane from (111) to (200). Most tendencies observed in TiN films are explained by the extended structure zone model (ESZM)[13].

In $Ti_{(1-x)}Al_xN$ coatings obtained via magnetron sputtering, the change in preferential orientation can also be influenced by the decreased Al fraction with increased substrate bias voltage[14]. According to PalDey and Deevi[18], the increase in substrate bias voltage causes a reduction in Al fraction due to the re-sputtering effect. As the Al atoms are lighter than the

Table 1. Correlation between the parameters and the preferential orientation.

Process Parameter	Coating	Change in preferential orientation with parameter increase	References
N_2 flow	TiN	(111) to (200)	12,13
N_2 partial pressure	TiN	(111) to (200)	13
Substrate temperature	TiN	(111) to (200)	13
Substrate bias voltage	$Ti_{(1-x)}Al_xN$	(111) to (200)	3,14
Aluminum fraction	$Ti_{(1-x)}Al_xN$	(200) to (111)	15
Film thickness	TiN	Amorphous, (200) to (111)	13,16

Ti atoms, the high-energy ions incident on the film selectively pulverizes the Al atoms. In this case, the plane (200) develops preferentially[14]. On the other hand, in a solid solution, replacing titanium (Ti) atoms with aluminum (Al) atoms leads to a deformation of the crystal lattice. As a result, the deformation energy gradually increases, and the plane (111) is favored[15].

When the titanium-based nitrides reach a critical thickness, the intensity of the (200) plane decreases, and a change from the preferential (200) plane to (111) takes place. Since the total deformation energy is expressed by the intrinsic deformation energy multiplied by the film thickness, the total deformation energy increases with the increase of film thickness. After exceeding the critical thickness of the films, the (111) orientation is favored[13].

Therefore, this work aimed to investigate the relations between the process parameters and crystallographic orientation of $Ti_{(1-x)}Al_xN$ films deposited in the metal mode (MM films) and the compound mode (CM films) through reactive grid-assisted magnetron sputtering (GAMS) deposition on silicon, copper, and plasma nitrided AISI D2 tool steel.

2. Experimental Details

2.1. Substrate and target materials

Monocrystalline silicon plates (100), copper, and AISI D2 tool steel cylinders were used as substrates. Silicon samples were cleaved into a rectangular shape of approximately (20 ± 2) mm x (15 ± 2) mm x 0.6 mm thick. Silicon was used to determine the average coating thickness and to analyze the coating chemical composition.

Copper substrates have a diameter of 3.0 mm, a thickness of (90 ± 10) μm, and a spherical hubcap with a thickness of (20 ± 5) μm. The copper substrates allowed the analysis of the microstructure of the coatings and selected area electron diffraction (SAED) patterns.

The steel cylinders have a diameter of 15.9 mm and a thickness of (9.8 ± 0.1) mm. The steel was used to measure the hardness (H) and elastic modulus (E) and determine the crystalline structure.

Table 2 overviews the substrates used and the characterization procedures performed.

The sputtering target was $Ti_{0.5}Al_{0.5}$ (99.50% purity), nominal composition by weight, from the manufacturer Able Target Limited. The target consists of a metal disk with a diameter of 100 mm and a thickness of 6 mm.

Table 2. Substrates and characterization techniques.

Substrates	Characterization techniques
Silicon	SEM, XPS
Copper	SAED – TEM
Plasma nitrided AISI D2 steel	XRD, IIT

2.2. Deposition process

The following cleaning procedures for the surfaces of the substrates were conducted:

- The silicon surface was cleaned with neutral detergent and running water.
- The contaminants present in the copper were removed by precision ionic polishing with argon (Ar) ions.
- The steel surface was ground and polished with silicon carbide abrasive paper and abrasives based on aluminum oxide (Al_2O_3) particles. After polishing, the steel specimens were ultrasonically immersed in isopropanol for 10 minutes.

Then, the surface of the steel was treated by bright nitriding using direct current (DC) plasma. This treatment was conducted in an atmosphere containing 5% N_2, 74% hydrogen (H_2), and 21% Ar by volume for 120.0 ± 0.5 minutes. During bright nitriding, the substrate temperature, discharge current, and discharge voltage were kept constant at (500 ± 5) ºC, (240 ± 2) mA, and (762 ± 2) V, respectively. These parameters were chosen to prevent the formation of a compound layer, which has a detrimental effect on the mechanical properties of the surface.

The hysteresis curve of the deposition process was obtained by varying the N2 flow rate. During the recording of the hysteresis curve, substrate temperature, Ar flow rate, and discharge current were kept constant and set to (300 ± 5) ºC, (2.8 ± 0.1) sccm, and 2.00 A, respectively. N_2 e Ar flow rate was adjusted by thermal mass flow control.

Subsequently, $Ti_{(1-x)}Al_xN$ films were deposited using direct current (DC) GAMS in a stainless steel (SS) chamber with a diameter of 280 mm and a thickness of 240 mm. The magnetron is unbalanced type II. The SS grid was positioned in the glow discharge region and corresponds to the system's third electrode[19]. The target-grid and target-substrate distances were set at 20 mm and 80 mm, respectively.

Target cleaning discharge was performed before all depositions at an Ar flow rate of (2.8 ± 0.1) sccm at 2.00 A DC for (2.0 ± 0.5) minutes.

Table 3 shows the process parameters used.

Depositions were performed in the metal and compound modes using an N_2 flow of (7.2 ± 0.1) sccm (near the FCP) for MM films and (6.8 ± 0.2) sccm (near the SCP) for CM films.

The substrate temperature, discharge current, substrate bias voltage, and Ar flow rate were kept constant in both deposition modes and were (300 ± 5) ºC, 2.00 A, -50 VDC, and (2.8 ± 0.1) sccm, respectively.

2.3. Characterization of chemical and mechanical properties

The chemical and mechanical properties of the coatings were characterized by X-ray photoelectron spectroscopy (XPS), X-ray diffraction (XRD), scanning electron microscopy (SEM), transmission electron microscopy (TEM), and instrumented indentation technique (IIT).

The XPS spectra were acquired in a Thermo Scientific K-Alpha system. The samples were cleaned through ion gun sputtering for 240 seconds before measurement. The monochromated X-ray source used the Al Kα line (1486.6 eV), and the X-ray spot was 400 µm. Survey spectra were acquired for both samples in the energy range -10.00 eV to 1350.00 eV using a dwell time of 100 ms, pass energy of 100.00 eV, energy step size of 0.500 eV, and three scans. High-resolution spectra for Ti 2p (448.00 – 475.00 eV), Al 2p (65.00 – 85.00 eV), N 1s (392.00 – 410.00 eV) and O 1s (525.00 – 545.00 eV) were measured using dwell time of 100 ms, pass energy of 20.00 eV, energy step size of 0.025 eV and 10 scans. The films' chemical composition was obtained from the high-resolution spectra using the Avantage software from Thermo Scientific.

X-ray spectra were obtained using a Shimadzu XRD-6000 diffractometer with copper $K_{\alpha 1}$ radiation, a wavelength of 1.5406 Å, an energy of 40 keV, a current density of 30.0 mA, and a scanning speed of 2.0 º per minute. The spectra were processed using OriginPro software. The crystalline phases were identified based on the positions of the diffracted lines and the respective interplanar distances, which were compared with the inorganic crystal structure database (ICSD).

The microstructure and average coating thickness were analyzed using a scanning electron microscope (SEM) with a Jeol JSM - 670 1F field-effect electron gun. To determine the average film thickness, the silicon samples were fractured into a cross-section, and the images were processed using ImageJ software. Nine measurements were made per coating.

Surface images of the films and the selected area electron diffraction patterns (SAED) were obtained using TEM, model Jeol 2100. The acquired images were processed using ImageJ software. From the surface images of the coatings, it was possible to determine the apparent size of the crystallites. For this purpose, 60 measurements were made per coating, and the five largest and five smallest values were not considered when calculating the apparent size of the crystallites. The crystalline structure of the coatings was determined from the images obtained via SAED-TEM. The interplanar distances were calculated from the mean diameter of the diffracted rings. The crystal structure of the studied regions was determined by comparing the interplanar distances with the ICSD database.

The hardness and elastic modulus of the coatings were determined using the CETR nanoindenter in conjunction with the atomic force microscope. A Berkovich diamond was used as the tip. The tip of the indenter penetrated a maximum of 10% of the total thickness of the coatings. The Poisson's ratio (ν) of the coatings was assumed to be 0.26[20]. Thirty-two indentations were performed with a load of 7.0 mN. The two highest and the two lowest measured values were not considered when calculating the average.

3. Results and Discussion

3.1. Hysteresis process

Figure 1a shows that the pressure curves corresponding to the increase and decrease in N_2 flow rate do not overlap, characterizing the hysteresis process.

Table 3. Process parameters.

Deposition mode	N_2 flow (sccm)	Pressure (Pa)	Voltage (V)	Time (min)
Metal	7.2 ± 0.1	0.50	492 ± 2	25.0 ± 0.5
Compound	6.8 ± 0.2	0.90	418 ± 23	60.0 ± 0.5

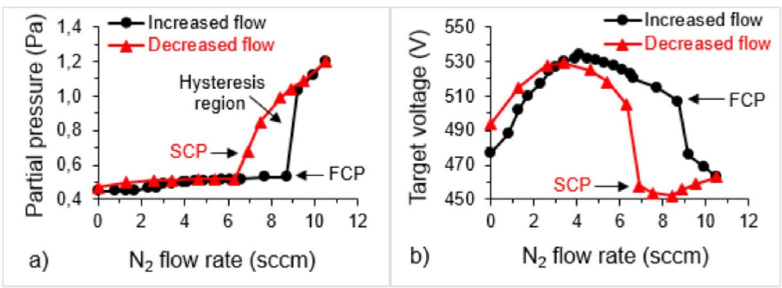

Figure 1. Hysteresis curve of the $Ti_{(1-x)}Al_xN$ reactive deposition process using a DC power supply as a function of (a) N_2 partial pressure and (b) target voltage.

Table 4. Coating chemical composition, in atomic percent, via XPS.

Deposition mode	Titanium (at %)	Aluminum (at %)	Nitrogen (at %)	Oxygen (at %)
Metal	19	29	39	13
Compound	19	27	38	16

Table 5. Ti-Al target chemical composition, in atomic percent, via XPS.

Chemical element	(at %)
Titanium	31
Aluminum	53
Oxygen	16

At low N_2 flow rate, all the reactive gas is gettered by the Ti and Al atoms ejected from the target. Consequently, the partial pressure practically does not change, and the sputtering yield is high[21]. At about (8.7 ± 0.1) sccm, the partial pressure of N_2 changes abruptly due to a slight change in the reactive gas flow. The target is "poisoned", the consumption of reactive gas decreases, and the sputtering yield is low. Decreasing the N_2 flow rate, the compound mode persists until about (6.4 ± 0.1) sccm, after which the deposition changes to metal mode.

The increase in the target voltage at the beginning of the hysteresis curve (Figure 1b) can be related to the formation of TiN on the target surface. The surface is still predominantly metal[11,22], but TiN promotes a secondary electron yield lower than metal Ti[23]. Therefore, to sustain a constant discharge current during TiN formation, the plasma must operate at a higher voltage[11]. The observed voltage drop around (4.2 ± 0.1) sccm is related to the increase of AlN content in the compound. Aluminum nitride has a higher secondary electron emission coefficient than metal Al[23]. Therefore, the system requires a lower voltage to maintain the same current[11,23,24].

Another factor that may have influenced the formation of TiN and AlN phases in the target is the Gibbs free energy. The free energy of the formation of TiN (-339 $kJ.mol^{-1}$) is lower than that of AlN (-319 $kJ.mol^{-1}$)[25]. Therefore, considering only the Gibbs free energy of the nitrides, TiN would first be formed on the surface of the target.

3.2. Chemical composition

Table 4 and 5 show the fraction of the constituent elements of the films and the Ti-Al target in atomic percent. In addition to the constituent elements of the target and the reactive gas used, it is observed that the films have oxygen in their chemical composition.

No significant differences were observed in Al 2p and O 1s spectra for both samples, indicating the formation of Al-N and metal oxide, respectively. The Ti 2p spectra (Figure 2) present the typical structure for $Ti_{(1-x)}Al_xN$ films with the Ti 2p core-level peaks and a satellite structure. This satellite is observed in TiN films and grows relative to Ti 2p core-level peaks with the addition of Al[26]. Considering that both films have, in practice, the same Al content, the most pronounced "satellite peak" observed in the compound film can have a contribution of Ti-O-N bonds[27].

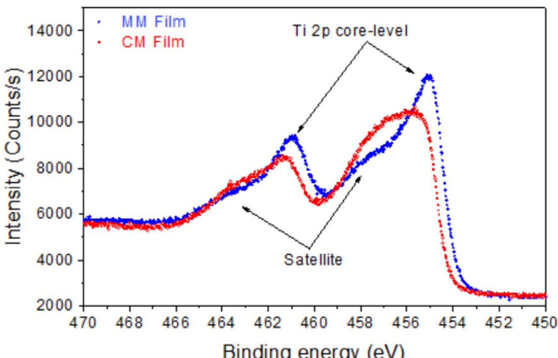

Figure 2. Ti 2p spectra for MM and CM films.

The fitting of N 1s spectra (Figure 3a and 3b) using Gaussian-Lorentzian sum curves (70% Lorentzian) shows the contribution of N in $Ti_{1-x}Al_xN$ and N in TiAl oxynitrides bonds[27], with a slight increase in the contribution of oxynitrides for the compound film (13% for MM film and 16% for CM film). The background was removed using the Shirley method and the Smart routine from the Avantage software.

Since the DRX and SAED measurements do not indicate the presence of oxynitrides, this is probably due to surface oxidation.

3.3. Crystallographic texture

Figure 4 shows X-ray diffraction patterns in both films which correspond to the tetragonal nitrogen-martensite (α'-$Fe_{(N)}$) phase[28,29] with preferential (110) plane and the $Ti_{(1-x)}Al_xN$ (ICSD-58012) with face-centered cubic (FCC) structure (space group 225). The X-ray spectra did not show diffraction lines approaching the AlN phase with compact hexagonal structure, nor did they detect diffraction lines referring to oxide or oxynitride.

For $Ti_{(1-x)}Al_xN$ coatings with Al contents below the solubility limit of the cubic phase, the X-ray diffraction pattern of $Ti_{(1-x)}Al_xN$ is almost identical to that of TiN - FCC, except for the position of the diffraction lines. In solid solution, the Al atoms replace the Ti atoms in the TiN crystal lattice. Since Al (R_{Al} = 0.143 nm) has a smaller atomic radius than Ti (R_{Ti} = 0.147 nm)[30], the replacement of Ti atoms with Al atoms leads to a decrease in the lattice parameter of the unit cell $Ti_{(1-x)}Al_xN$, and the diffraction lines shift to higher values 2θ[31,32]. The $Ti_{(1-x)}Al_xN$ phase with the FCC structure (space group 225) is usually formed in $Ti_{(1-x)}Al_xN$ films whose Al content is less than 0.65. At Al concentrations equal to or greater than 0.65, the formation of TiN - FCC and AlN - HC "wurtzite" phases may occur[11,33-36].

An important analysis concerns crystallographic orientation. The X-ray spectra in Figure 4 reveal a preferential evolution of (111) plane in the MM films and (200) in the CM films.

Table 6. Average film thickness deposited on silicon. Images obtained via SEM.

Deposition mode	Average thickness (µm)	Deposition time (min)	Deposition rate (nm/min)
Metal	1.2 ± 0.1	25.0 ± 0.5	48 ± 2
Compound	0.9 ± 0.1	60.0 ± 0.5	15 ± 1

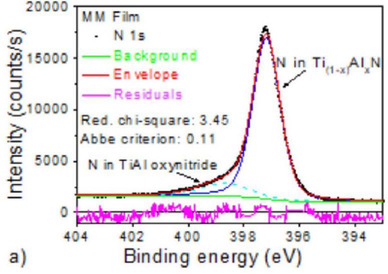

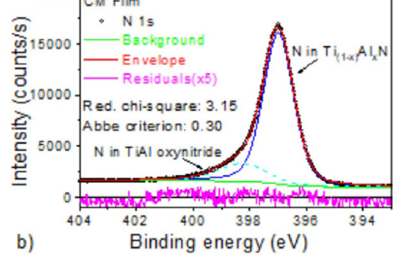

Figure 3. N 1s fitted spectra for (a) MM film and (b) CM film.

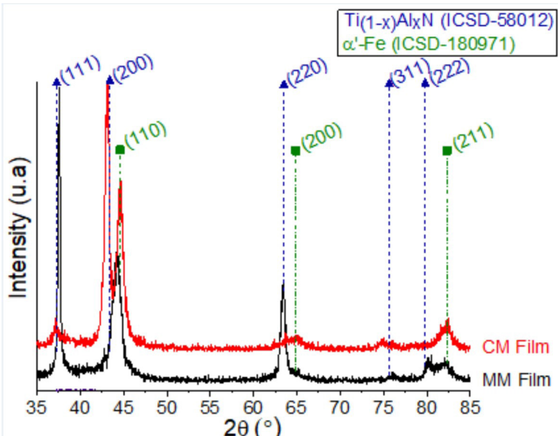

Figure 4. XRD pattern of MM and CM films.

The films deposited at compound mode have an Al content of 27 (at %) and an average thickness of (0.9 ± 0.1) µm. Films grown in metal mode have an Al content of about 29 (at %), with an average thickness of (1.2 ± 0.1) µm (Table 4 and 6). Increasing the film thickness above a certain critical thickness might have influenced the development of the (111) plane in the MM films. The total deformation energy of titanium nitride increases with increasing film thickness, favoring the preferential plane (111) (see section 1)[13].

Both coatings were deposited using the same substrate bias voltage (-50 VDC) and substrate temperature (300 ± 5) ºC, therefore these parameters should not have affected the change in plane orientation.

However, the atomic N/Ti flux and the reactive gas partial pressure are determinant factors for changing the preferential orientation of the TiN and $Ti_{(1-x)}Al_xN$ films. This work used total pressure of about 0.50 Pa for depositions in metal mode and 0.90 Pa for depositions in compound mode, being the difference due to the increase in N_2 partial pressure. Since the reactive gas pressure affects the atomic N/Ti flux, the preferential orientation transition between the (111) and (200) planes results from the difference in the adatoms diffusion length with the increased atomic N/Ti flux. Intense flows provide a higher diffusion length, affecting grain growth and favoring the development of the (200) plane[13].

It can be seen from the SEM image that the column sizes of the coatings are larger in the metal mode (Figure 5a) than in the compound mode (Figure 5c). The SEM images of the microstructure in Figure 5b and 5d show that both films correspond to zone T of the ESZM, which consists of dense and compact columns[13].

MM films exhibited preferential (111) plane orientation, while CM films had preferential (200) plane orientation. According to Mahieu and Depla[13], TiN microstructure and crystallographic orientation have a significant relationship. The type of reactive gas acting in the depositions explains this relationship. In the microstructures corresponding to zone T, the (111) plane develops favorably when the depositions are carried out with a lower atomic N/Ti flux. In this case, the reactive gas acts as a molecular gas (N_2). However, when depositions are performed with a higher atomic N/Ti flux, the reactive gas acts as atomic gas (N), and favorable growth in (200) orientation is developed[13].

Table 6 shows the average film thickness and deposition rate. The lower value of deposition rate for CM films compared to MM films is related to the decrease of sputtering yield with target poisoning. With a larger supply of reactive gas in the discharge chamber, the Ti and Al atoms in the target combined with the reactive gas and formed compounds on its surface. As a result, films with lower deposition rates are formed[9,11].

The grain characteristic and the formed phases in the coatings deposited on the copper disks were analyzed. This analysis uses normal section surface images and the SAED technique. Both images were obtained via TEM (Figure 6) and processed using ImageJ and Process Diffraction software.

The apparent size of the crystallites was determined from normal section surface images (TEM). Grains were found with an average size of (29 ± 5) nm for MM films and (65 ± 7) nm for CM films.

As for the surface, granular features are observed in both modes, and grains with irregular shapes predominate in the compound mode. The irregular grain shape could result from the lower atomic mobility in this deposition regime and influences the formation of voids or gaps, reducing the grain boundary area[37]. In earlier models, the influence of energy flux to the substrate on film growth is discussed. For example, in TiN films, a lower deposition rate leads to a lower energy flux towards the substrate and, consequently, to lower atomic mobility[13].

The SAED images show the presence of characteristic rings of polycrystalline materials. The $Ti_{(1-x)}Al_xN$ phase (ICSD-58012) with FCC structure (space group 225) was formed in both coatings. However, the interplanar distances (Table 7) suggest regions rich in AlN - FCC crystals (ICSD-41358) in the metal mode (Figure 6b) and TiN - FCC crystals (ICSD-152807) in the compound mode (Figure 6d). The incorporation of AlN precipitates in $Ti_{(1-x)}Al_xN$ films may be related to the formation of smaller grain sizes in the metal mode[35]. It has been observed that the distances between adjacent planes have increased when compared to the reference sheet of the AlN - FCC phase (ICSD-41358). The increase in the interplanar distances could be due to the substitution of some Al atoms by Ti atoms in the AlN crystal lattice. These results refer to specific areas of the samples and are therefore not representative of the whole coating.

The results obtained by SAED agree with the X-ray diffraction spectra performed on steel, as shown in Figure 4.

Table 7 shows the parameters used to determine the phases present in the metal and compound coatings.

3.4. Hardness (H) and elastic modulus (E)

Table 8 shows the values of hardness (H) and elastic modulus (E). The mechanical properties were determined using the IIT.

Residual stress, chemical composition, crystallographic texture, and microstructure influence the hardness of materials[3,7,38]. Compared to the CM films, the MM films showed the highest hardness values, elastic modulus, and H^3/E^2 ratio (Table 8), resulting from the microstructure formed, and the preferential (111) plane.

The X-ray spectra (Figure 4) show the development of the preferential (200) plane in the compound mode and (111) in the metal mode. Since a (111) plane is more compact than a (200) plane, the crystallographic texture (111) might have contributed to the higher hardness values of the MM films[3,22].

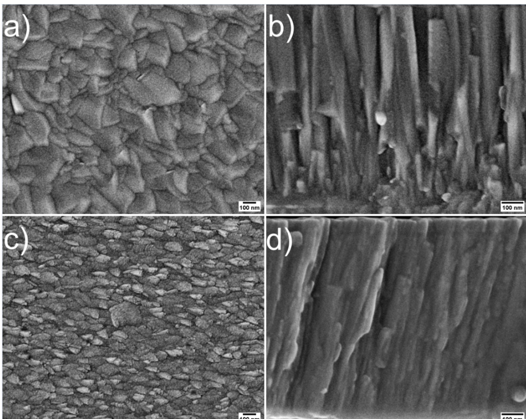

Figure 5. SEM images of film deposited at MM: (a) surface and (b) microstructure. SEM images of film deposited at CM: (c) surface and (d) microstructure.

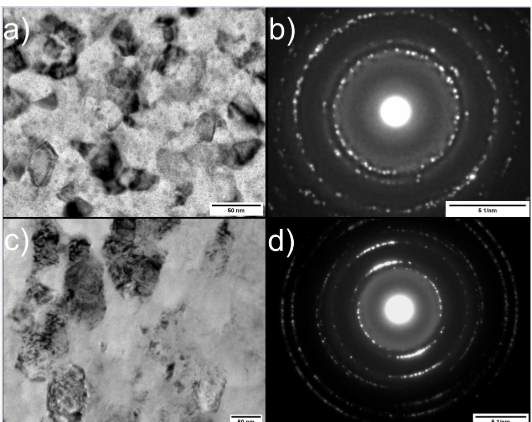

Figure 6. TEM Plan view: (a) MM films and (c) CM films. SAED-TEM: (b) MM films and (d) CM films.

Table 7. Interplanar distance of phases present in coatings grown at metal and compound modes via SAED-TEM.

Diffracted ring	Crystalline plane	MM films Interplanar distances (Å)	CM films Interplanar distances (Å)
1	(111)	2.40 ± 0.05	2.43 ± 0.05
2	(200)	2.08 ± 0.05	2.11 ± 0.05
3	(220)	1.47 ± 0.05	1.49 ± 0.05
4	(311)	1.25 ± 0.05	1.27 ± 0.05
5	(222)	1.20 ± 0.05	1.22 ± 0.05

Table 8. Hardens and elastic modulus via IIT.

Deposition mode	Hardness (GPa)	Elastic modulus (GPa)	H/E (GPa)	H^3/E^2 (.10^{-2} GPa)
Metal	23 ± 1	346 ± 17	6.5 ± 0.5	10 ± 1
Compound	17 ± 1	272 ± 18	6.4 ± 0.7	7 ± 1

The decrease in crystallite size leads to an increase in the grain boundary area. As a result, the propagation of cracks along the grain boundaries decreases, and the hardness of the material increases[3]. This phenomenon is known as the Hall-Pech effect. According to the Hall-Pech relationship, the hardness of coatings is inversely proportional to the square of the mean diameter of the grains. Therefore, the grain size might have influenced the higher hardness values of the MM coatings[3].

Table 8 shows no significant differences in the H/E ratio of the different films. However, the MM films have an H^3/E^2 ratio of (10 ± 1).10^{-2} GPa, and the compound mode films have an H^3/E^2 ratio of (7 ± 1).10^{-2} GPa. The H/E and H^3/E^2 ratios provide information about the fracture toughness and resistance to the material's plastic deformation[3,38,39]. Increasing the H^3/E^2 ratio increases the materials' resistance to plastic deformation[3,38]. Therefore, the H^3/E^2 ratio indicates that MM films have better resistance to plastic deformation than CM films.

4. Conclusion

The amount of Al present in the films influenced the crystalline phase's formation. The formation of $Ti_{(1-x)}Al_xN$ (ICSD-58012) phase with FCC structure (space group 225) was observed in both films. The crystalline phase resembles the B1-NaCl structure.

$Ti_{(1-x)}Al_xN$ films exhibited preferential (111) orientation in the metal mode and (200) in the compound mode. The change in crystallographic orientation is mainly related to the N_2 pressure present in the working atmosphere. The formation of thin columns and grains with regular shapes in the microstructure of the MM films was observed. On the other hand, compound mode films formed dense columns with irregular grains. The crystallographic orientation and resulting microstructure strongly depend on the process parameters used. The pressure of the reactive gas present in the working atmosphere differentiated the depositions. The increase of N_2 partial pressure in compound mode leads to a higher N/Ti atomic flux, favoring the (200) plane.

The higher hardness and H^3/E^2 ratio values in metal mode coatings are attributed to the microstructure formed and the preferential development of the crystallographic (111) texture.

5. Acknowledgments

This work was supported by the Santa Catarina State research funding agency (FAPESC) through the program PAP in association with the Santa Catarina State University under contract PAP-TR 655. Part of the funding for this study came from the UNIEDU/FUMDES graduate program. The authors acknowledge the structural support provided by Santa Catarina State University (UDESC), Brazil; Plasma Lab Facility (LPFS), Brazil.

6. References

1. Mitterer C, Holler F, Üstel F, Heim D. Application of hard coatings in aluminum die casting-soldering, erosion and thermal fatigue behavior. Surf Coat Tech. 2000;125:233-9. http://dx.doi.org/10.1016/S0257-8972(99)00557-5.
2. Podgornik B, Zajec B, Bay N, Vižintin J. Application of hard coatings for blanking and piercing tools. Wear. 2011;270:850-6. http://dx.doi.org/10.1016/j.wear.2011.02.013.
3. Devia DM, Restrepo-Parra E, Arango PJ, Tschiptschin AP, Velez JM. TiAlN coatings deposited by triode magnetron sputtering varying the bias voltage. Appl Surf Sci. 2011;257:6181-5. http://dx.doi.org/10.1016/j.apsusc.2011.02.027.
4. Hörling A, Hultman L, Odén M, Sjölén J, Karlsson L. Mechanical properties and machining performance of $Ti_{1-x}Al_x$ N-coated cutting tools. Surf Coat Tech. 2005;191:384-92. http://dx.doi.org/10.1016/j.surfcoat.2004.04.056.
5. Kawata K, Sugimura H, Takai O. Characterization of (Ti,Al)N films deposited by pulsed d.c. plasma-enhanced chemical vapor deposition. Thin Solid Films. 2001;386:271-5. http://dx.doi.org/10.1016/S0040-6090(00)01672-2.
6. Hsieh JH, Liang C, Yu CH, Wu W. Deposition and characterization of TiAlN and multi-layered TiN/TiAlN coatings using unbalanced magnetron sputtering. Surf Coat Tech. 1998;108-109:132-7. http://dx.doi.org/10.1016/S0257-8972(98)00684-7.
7. Barshilia HC, Rajam KS. Reactive sputtering of hard nitride coatings using asymmetric-bipolar pulsed DC generator. Surf Coat Tech. 2006;201:1827-35. http://dx.doi.org/10.1016/j.surfcoat.2006.03.012.
8. Zhang Y, Yan X, Liao W, Zhao K. Effects of nitrogen content on the structure and mechanical properties of $(Al_{0.5}CrFeNiTi_{0.25})N_x$ high-entropy films by reactive sputtering. Entropy (Basel). 2018;20:602. http://dx.doi.org/10.3390/e20090624.
9. Berg S, Nyberg T. Fundamental understanding and modeling of reactive sputtering processes. Thin Solid Films. 2005;476:215-30. http://dx.doi.org/10.1016/j.tsf.2004.10.051.

10. Berg S, Särhammar E, Nyberg T. Upgrading the "Berg-model" for reactive sputtering processes. Thin Solid Films. 2014;565:186-92. http://dx.doi.org/10.1016/j.tsf.2014.02.063.
11. Arif M, Sauer M, Foelske-Schmitz A, Eisenmenger-Sittner C. Characterization of aluminum and titanium nitride films prepared by reactive sputtering under different poisoning conditions of target. J Vac Sci Technol A. 2017;35:1-10. http://dx.doi.org/10.1116/1.4993082.
12. Lu L, Luo F, Huang Z, Zhou W, Zhu D. Influence of the nitrogen flow rate on the infrared emissivity of TiNx films. Infrared Phys Technol. 2018;88:144-8. http://dx.doi.org/10.1016/j.infrared.2017.11.015.
13. Mahieu S, Depla D. Reactive sputter deposition of TiN layers: modelling the growth by characterization of particle fluxes towards the substrate. J Phys D Appl Phys. 2009;42:1-16. http://dx.doi.org/10.1088/0022-3727/42/5/053002.
14. Elmkhah H, Zhang TF, Abdollah-zadeh A, Kim KH, Mahboubi F. Surface characteristics for the TiAlN coatings deposited by high power impulse magnetron sputtering technique at the different bias voltages. J Alloys Compd. 2016;688:820-7. http://dx.doi.org/10.1016/j.jallcom.2016.07.013.
15. He C, Zhang J, Song G, Ma G, Du Z, Wang J, et al. Microstructure and mechanical properties of reactive sputtered nanocrystalline (Ti,Al)N films. Thin Solid Films. 2015;584:192-7. http://dx.doi.org/10.1016/j.tsf.2014.12.027.
16. Olia H, Ebrahimi-Kahrizsangi R, Ashrafizadeh F, Ebrahimzadeh I. Comparative study of corrosion and corrosion-wear behavior of TiN and CrN coatings on UNS S17400 stainless steel. Corros Rev. 2018;36:403-12. http://dx.doi.org/10.1515/corrrev-2017-0130.
17. Ajenifuja E, Popoola API, Popoola OM. Thickness dependent chemical and microstructural properties of DC reactive magnetron sputtered titanium nitride thin films on low carbon steel cross-section. J Mater Res Technol. 2019;8:377-84. http://dx.doi.org/10.1016/j.jmrt.2018.02.010.
18. PalDey S, Deevi SC. Single layer and multilayer wear resistant coatings of (Ti,Al)N: a review. Mater Sci Eng A. 2003;342:58-79. http://dx.doi.org/10.1016/S0921-5093(02)00259-9.
19. Fontana LC, Muzart JRL. Triode magnetron suttering TiN film deposition. Surf Coat Tech. 1999;114:7-12. http://dx.doi.org/10.1016/S0257-8972(99)00032-8.
20. He Y, Schwarz BR, Migliori AE. Elastic constants of single crystal y – TiAl. J Mater Res. 1995;10:1187-95. http://dx.doi.org/10.1557/JMR.1995.1187.
21. Rohde SL, Münz DW. Sputter deposition. In: Rickerby DS, Matthews A, editors. Advanced surface coatings: a handbook of surface engineering. Glasgow: Blackie; 1991. p. 92-126.
22. Gao F, Li G, Xia Y. Influence of hysteresis effect on properties of reactively sputtered TiAlSiN films. Appl Surf Sci. 2018;431:160-4. http://dx.doi.org/10.1016/j.apsusc.2017.07.283.
23. Lewis MA, Glocker AD, Jacob J. Measurements of secondary electron emission in reactive sputtering of aluminum and titanium nitride. J Vac Sci Technol A. 1989;7:1019-24. http://dx.doi.org/10.1116/1.576222.
24. Depla S, Li XY, Mahieu S, De Gryse R. Determination of the effective electron emission yields of compound materials. J Phys D Appl Phys. 2008;41:1-4. http://dx.doi.org/10.1088/0022-3727/41/20/202003.
25. Shew BY, Huang JL. The effects of nitrogen flow on reactively sputtered Ti-Al-N films. Surf Coat Tech. 1995;71:30-6. http://dx.doi.org/10.1016/0257-8972(94)02300-F.
26. Greczynski G, Jensen J, Greene JE, Petrov I, Hultman L. X-ray photoelectron spectroscopy analyses of the electronic structure of polycrystalline Ti 1-x Al x N thin films with $0 \leq x \leq 0.96$. Surf Sci Spectra. 2014;21:35-49. http://dx.doi.org/10.1116/11.20140506.
27. Marco JF, Gancedo JR, Auger MA, Sánchez O, Albella JM. Chemical stability of TiN, TiAlN and AlN layers in aggressive so 2 environments. Surf Interface Anal. 2005;37:1082-91. http://dx.doi.org/10.1002/sia.2083.
28. Díaz-Guillén JC, Naeem M, Hdz-García HM, Acevedo-Davila JL, Díaz-Guillén MR, Khan MA, et al. Duplex plasma treatment of AISI D2 tool steel by combining plasma nitriding (with and without white layer) and post-oxidation. Surf Coat Tech. 2020;385:1-14. http://dx.doi.org/10.1016/j.surfcoat.2020.125420.
29. Jacobsen SD, Hinrichs R, Baumvol IJR, Castellano G, Vasconcellos MAZ. Depth distribution of martensite in plasma nitrided AISI H13 steel and its correlation to hardness. Surf Coat Tech. 2015;270:266-71.
30. Knotek O, Bohmer N, Leyendecker T. On structure and properties of sputtered Ti and Al based hard compound films. J Vac Sci Technol A. 1986;2:2695-700. http://dx.doi.org/10.1116/1.573708.
31. Asgary S, Ghoranneviss M, Mahmoodi A, Zareindolab Z. Evolution of structural, morphological, mechanical and optical properties of TiAlN coastings by variation of N and Al Amount. J Inorg Organomet Polym. 2018;28:428-38. http://dx.doi.org/10.1007/s10904-017-0603-z.
32. Giuliani F, Ciurea C, Bhakhri V, Werchota M, Vandeperre LJ, Mayrhofer PH. Deformation behaviour of TiN and Ti–Al–N coatings at 295 to 573 K. Thin Solid Films. 2019;688:1-7. http://dx.doi.org/10.1016/j.tsf.2019.06.013.
33. Santana AE, Karimi A, Derflinger VH, Schütze A. Thermal treatment effects on microstuture and mechanical properties of TiAlN thin films. Tribol Lett. 2004;17:689-96. http://dx.doi.org/10.1007/s11249-004-8074-0.
34. Abrikosov IA, Knutsson A, Alling B, Tasnádi F, Lind H, Hultman L, et al. Phase stability and elasticity of TiAlN. Mater. 2011;4:1599-618. http://dx.doi.org/10.3390/ma4091599.
35. Pemmasani SP, Valleti K, Gundakaram RC, Rajulapati KV, Mantripragata R, Koppoju S, et al. Effect of microstructure and phase constitution on mechanical properties of $Ti_{1-x}Al_xN$ coatings. Appl Surf Sci. 2014;313:936-46. http://dx.doi.org/10.1016/j.apsusc.2014.06.112.
36. Yoshikawa M, Toyama D, Fujita T, Nagatomo N, Makimoto T. Hole conduction characteristics of cubic $Ti_{1-x}Al_xN$. Thin Solid Films. 2018;660:711-4. http://dx.doi.org/10.1016/j.tsf.2018.04.010.
37. Liu ZJ, Shen YG. Effects of Al content on grain growth of solid solution (Ti,Al)N films. J Vac Sci Technol A. 2006;24:174-7. http://dx.doi.org/10.1116/1.2148416.
38. Musil J, Jirout M. Toughness of hard nanostructured ceramic thin films. Surf Coat Tech. 2007;201:5148-52. http://dx.doi.org/10.1016/j.surfcoat.2006.07.020.
39. Recco AAC, Oliveira IC, Massi M, Maciel HS, Tschiptschin AP. Adhesion of reactive magnetron sputtered TINx and TICy coatings to AISI H13 tool steel. Surf Coat Tech. 2007;202:1078-83. http://dx.doi.org/10.1016/j.surfcoat.2007.07.073.